VII International Conference on Computational Methods for Coupled Problems in Science and Engineering
COUPLED PROBLEMS 2017
M. Papadrakakis, E. Oñate and B. Schrefler (Eds)

FLUID-STRUCTURE INTERACTION MODELING OF ARTERY ANEURYSMS WITH STEADY-STATE CONFIGURATIONS

Eugenio Aulisa*, Giorgio Bornia† and Sara Calandrini†

* Department of Mathematics and Statistics
Texas Tech University
Lubbock, TX 79409, USA
e-mail: eugenio.aulisa@ttu.edu

† Department of Mathematics and Statistics
Texas Tech University
Lubbock, TX 79409, USA
e-mail: giorgio.bornia@ttu.edu, sara.calandrini@ttu.edu

Key words: Cerebral aneurysms, Incompressible Navier-Stokes equations, Fluid-structure interaction, Intracranial stent.

Abstract. This paper addresses numerical simulations of fluid-structure interaction (FSI) problems involving artery aneurysms, focusing on steady-state configurations. Both the fluid flow and the hyperelastic material are incompressible. A monolithic formulation for the FSI problem is considered, where the deformation of the fluid domain is taken into account according to an Arbitrary Lagrangian Eulerian (ALE) scheme. The numerical algorithm is a Newton-Krylov method combined with geometric multigrid preconditioner and smoothing based on domain decomposition. The system is modeled using a specific equation shuffling that aims at improving the row pivoting. Due to the complexity of the operators, the exact Jacobian matrix is evaluated using automatic differentiation tools. We describe benchmark settings which shall help to test and compare different numerical methods and code implementations for the FSI problem in hemodynamics. The configurations consist of realistic artery aneurysms. A case of endovascular stent implantation on a cerebral aneurysm is also presented. Hybrid meshes are employed in such configurations. We show numerical results for the described aneurysm geometries for steady-state boundary conditions. Parallel implementation is also addressed.

1 INTRODUCTION

Over the last decade numerous advances in the simulation of stented brain aneurysms were proposed, but the majority of them involved only computational fluid dynamics

(CFD). When pure CFD is used for vascular blood flow simulations, it is assumed that the vessel wall remains rigid. The rigid wall assumption does not properly reflect the elastic nature of arterial walls and the behavior of real blood vessels, since vessel walls are deformed by the action of blood flow forces and, in turn, this deformation alters the details of blood flow. For the modeling to be realistic, coupled fluid-structure interaction (FSI) modeling must be employed. In this work, we propose FSI simulations of stenting technology applied to 2D and 3D brain aneurysms geometries. We consider a monolithic coupling between the fluid and the solid, focusing on steady-state formulations. Blood has been considered as an incompressible Newtonian fluid and a hyperelastic solid has been used to represent vessel wall tissue. We describe the solid motion in a Lagrangian way, while the fluid is observed in Eulerian fashion. The deformation of the fluid domain is taken into account according to an Arbitrary Lagrangian Eulerian (ALE) approach, which is one of the most popular techniques in the FSI community ([3], [6], [11]). To solve the FSI system, we propose a monolithic Newton-Krylov solver preconditioned by a geometric multigrid algorithm. Newton linearization is performed as an outer iteration, and the the evaluation of the exact Jacobian matrix associated to the fluid-solid coupled state equations is performed with automatic differentiation tools provided by the Adept software package ([8]). Multigrid F-cycle and V-cycle schemes are considered with a Richardson smoother preconditioned by an additive Schwarz method (ASM). Other works in which multigrid and domain decomposition methods are employed for hemodynamics applications are [10], [9] and [12]. Our solver has been implemented in the open-source *C++ Femus library* (https://github.com/FeMTTU/femus) using the GMRES solver and the geometric multigrid preconditioner interface implemented in the PETSc toolkit [4]. For validation and evaluation of the accuracy and performance of the proposed methodology, we present numerical studies for both 2D and 3D cerebral aneurysm configurations. To simulate the effect of stents, we consider both the meshing of flow diverters and the porous medium (PM) approach ([2]). Advantages of the porous medium method include the reduction of the number of simulation mesh elements, with the resulting reduction of computational time. The paper is organized as it follows. In Section 2 we present the strong formulations of the steady-state incompressible FSI problem under investigation. In section 3 we describe our Monolithic Newton-Krylov solver. Numerical results of benchmark problems are presented in Sections 4 and 5. Finally, we draw our conclusions.

2 FORMULATION OF THE FSI PROBLEM

Let $\Omega = \Omega^f \cup \Omega^s \subset \mathbb{R}^n$ be the current configuration of fluid and solid at time $T = \infty$. Clearly, Ω^f and Ω^s are referred to fluid and solid, respectively. Let $\Gamma^i = \Omega^f \cap \Omega^s$ be the interface between solid and fluid in the current configuration, and let Γ^f and Γ^s be the parts of the boundary adjacent only to the fluid or only to the solid.
We use the *hat* notation to define $\widehat{\Omega}^f := \Omega_0^f$ and $\widehat{\Omega}^s := \Omega_0^s$. Normally, they are referred to as the undeformed or reference configuration. Consequently, we define $\widehat{\Omega} := \Omega_0$ and $\widehat{\Gamma}^i := \Gamma_0^i$. In the following we will use the notations $\widehat{\nabla}$ or ∇ to refer to the gradient

operators and the symbols $\widehat{\mathbf{n}}$ or $\mathbf{n}$ to denote the outward unit normal fields in the reference or in the current configuration, respectively.
The domain $\widehat{\Omega}^s$ is called *Lagrangian domain* and the field $q^s(\widehat{\mathbf{x}})$ defined on it is called *Lagrangian field*. Furthermore, the domain $\widehat{\Omega}^f$ is called *ALE domains* and the field $q^f(\widehat{\mathbf{x}})$ defined on it is called *ALE field*. We remark that $\widehat{\Omega}^s$, $\widehat{\Omega}^f$ were initially occupied only by the solid and fluid, respectively. As a consequence of the solid movement, the domain on which we observe the fluid motion changes, and we need to define a deformation for the fluid domain. The domain Ω^f is occupied only by fluid at time $T = \infty$. The moving domains Ω^f and Ω^s are called *Eulerian domains*, and fields $q(\mathbf{x})$ defined on Eulerian domains are called *Eulerian fields*. Notice that the Eulerian domains dipends on the current configuration at time $T = \infty$. In order to describe the motion of the fluid and solid domains, let us define an invertible and sufficiently smooth mapping $\mathcal{X}$, so that

$$\mathcal{X} : \widehat{\Omega} \to \Omega\,, \quad \mathcal{X}(\widehat{\mathbf{x}}) := \widehat{\mathbf{x}} + \mathbf{d}(\widehat{\mathbf{x}})\,. \tag{1}$$

The field $\mathbf{d}(\widehat{\mathbf{x}})$ is called *displacement field*. The displacement field $\mathbf{d}(\widehat{\mathbf{x}})$ is determined separately in the fluid and solid parts as a solution of two different subproblems. Its restrictions $\mathbf{d}^f(\widehat{\mathbf{x}})$ and $\mathbf{d}^s(\widehat{\mathbf{x}})$ are referred to as *fluid domain displacement* (or *ALE displacement*) and *solid displacement*, respectively. They are required to take on common values at the interface, namely

$$\mathbf{d}^s(\widehat{\mathbf{x}}) = \mathbf{d}^f(\widehat{\mathbf{x}})\,, \quad \widehat{\mathbf{x}} \in \widehat{\Gamma}^i\,. \tag{2}$$

For every $\widehat{\mathbf{x}} \in \widehat{\Omega}$, we also define

$$\mathbf{F}(\mathbf{d}(\widehat{\mathbf{x}})) = \widehat{\nabla}\mathcal{X}(\widehat{\mathbf{x}}) = I + \widehat{\nabla}\mathbf{d}(\widehat{\mathbf{x}})\,, \tag{3}$$

$$J(\mathbf{d}(\widehat{\mathbf{x}})) = \det \mathbf{F}(\mathbf{d}(\widehat{\mathbf{x}}))\,, \tag{4}$$

$$\mathbf{B}(\mathbf{d}(\widehat{\mathbf{x}})) = \mathbf{F}(\mathbf{d}(\widehat{\mathbf{x}}))\mathbf{F}^T(\mathbf{d}(\widehat{\mathbf{x}}))\,. \tag{5}$$

The symbols $\mathbf{F}$ and $\mathbf{B}$ denote the *deformation gradient tensor* and the *left Cauchy-Green deformation tensor*, respectively.

Steady-state solid subproblem. The steady-state solid subproblem consists in finding $(\mathbf{d}^s(\mathbf{x}), p^s(\mathbf{x}))$ such that

$$-\nabla \cdot \boldsymbol{\sigma}^s(\mathbf{d}^s, p^s) - \rho^s \mathbf{f}^s = \mathbf{0}\,, \quad \mathbf{x} \in \Omega^s\,, \tag{6}$$

$$J(\mathbf{d}^s) - 1 = 0\,, \quad \widehat{\mathbf{x}} \in \widehat{\Omega}^s\,, \tag{7}$$

$$\boldsymbol{\sigma}^s(\mathbf{d}^s, p^s) \cdot \mathbf{n}^s - \boldsymbol{\sigma}^f\left(\mathbf{u}^f, p^f\right) \cdot \mathbf{n}^f = 0\,, \quad \mathbf{x} \in \Gamma^i, \tag{8}$$

$$\mathcal{B}^s(\mathbf{d}^s, p^s) = \mathbf{0}\,, \quad \mathbf{x} \in \Gamma^s \tag{9}$$

The first two equations are known as the incompressible elasticity equations. Here, the symbols ρ^s and $\mathbf{f}^s$ denote mass density and body force density for the solid, respectively. In Eq.(9) $\mathcal{B}^s$ denotes an abstract boundary operator for the solid external boundary Γ^s, which may correspond to Dirichlet, Neumann or other types of boundary conditions.

In this solid subproblem the pressure in the solid p^s is an internal variable and it does not have a clear physical meaning. It can be regarded mathematically as the Lagrange multiplier associated to the solid incompressibility constraint. For the solid stress tensor $\boldsymbol{\sigma}^s$ we consider incompressible Mooney-Rivlin, whose Lagrangian description is given for every $(\widehat{\mathbf{x}}, t) \in \widehat{\Omega}^s$ by

$$\boldsymbol{\sigma}^s_{MR}(\mathbf{d}^s, p^s) = -p^s\mathbf{I} + \mathbf{2C_1B(d^s)} - \mathbf{2C_2}(\mathbf{B(d^s)})^{-\mathbf{1}}\,, \tag{10}$$

where the constants C_1 and C_2 depend on the mechanical properties of the material. We remark that the input to this solid subproblem is the stress at the interface coming from the fluid part while the output is the displacement of the solid, namely $\mathbf{d}^s$.

Steady-state fluid subproblem. The steady-state fluid subproblem consists in searching for $(u^f(\mathbf{x}), p^f(\mathbf{x}))$ such that

$$\rho^f\left(\mathbf{u}^f \cdot \nabla \mathbf{u}^f\right) - \nabla \cdot \boldsymbol{\sigma}^f(\mathbf{u}^f, p^f) - \rho^f \mathbf{f}^f = \mathbf{0} \quad \mathbf{x} \in \Omega^f\,, \tag{11}$$

$$\nabla \cdot \mathbf{u}^f = 0\,, \quad \mathbf{x} \in \Omega^f\,, \tag{12}$$

$$\mathcal{B}^f(\mathbf{u}^f(\mathbf{x}), p^f(\mathbf{x})) = \mathbf{0}\,, \quad \mathbf{x} \in \Gamma^f \tag{13}$$

$$\mathbf{u}^f(\mathbf{x}, 0) = 0\,, \quad \mathbf{x} \in \widehat{\Omega}^f\,. \tag{14}$$

The first two equations are referred to as the incompressible Navier-Stokes equations. Here, the symbols ρ^f and $\mathbf{f}^f$ denote mass density and body force density for the fluid. In Eq. (14) $\mathcal{B}^s$ is an abstract boundary operator for the fluid boundary, similarly as before. The fluid stress tensor $\boldsymbol{\sigma}^f$ for incompressible Newtonian fluid flows is given as a Eulerian field for every $(\mathbf{x}, t) \in \Omega^f_t$ by

$$\boldsymbol{\sigma}^f(\mathbf{u}^f, p^f) = -p^f\mathbf{I} + \mu(\nabla \mathbf{u}^f + (\nabla \mathbf{u}^f)^T)\,, \tag{15}$$

where μ is the fluid viscosity. The input to the fluid subproblem is the displacement of the fluid domain and the outputs are both fluid velocity and fluid pressure, which are used to compute the stress at the interface for the solid subproblem.

Steady-state subproblem for the fluid domain displacement. The steady-state subproblem for the fluid domain displacement consists in finding $\mathbf{d}^f(\mathbf{x})$ such that

$$\widehat{\nabla} \cdot \left(k(\widehat{\mathbf{x}})(\widehat{\nabla}\mathbf{d}^f + (\widehat{\nabla}\mathbf{d}^f)^T)\right) = \mathbf{0}\,, \quad \widehat{\mathbf{x}} \in \widehat{\Omega}^f\,, \tag{16}$$

$$\mathbf{d}^f = \mathbf{d}^s\,, \quad \widehat{\mathbf{x}} \in \widehat{\Gamma}^i\,, \tag{17}$$

$$\mathcal{B}^{fd}(\mathbf{d}^f(\widehat{\mathbf{x}})) = \mathbf{0}\,, \quad \widehat{\mathbf{x}} \in \widehat{\Gamma}^f\,. \tag{18}$$

This subproblem is also referred to as the *kinematic equation* or the *pseudo-solid mapping*, as it defines the arbitrary motion of the fluid domain as another elastic solid. In Eq. (18) we denote with $\mathcal{B}^{fd}$ a general boundary operator which can be chosen arbitrarily depending on the problem at hand. The function $k(\widehat{\mathbf{x}})$ may be chosen to be a piecewise-constant

function discontinuous across the element boundary so that smaller elements in the mesh can be made stiffer. We decided to consider

$$k(\widehat{\mathbf{x}}) = \frac{1}{\mathrm{V}_{el(\widehat{\mathbf{x}})}}, \tag{19}$$

where V_{el} is the volume of the mesh element that contains the $\widehat{\mathbf{x}}$ coordinate.
We remark that the input of this subproblem is the displacement of the fluid-solid interface from the solid part, while the output is the displacement of the fluid domain.

If we compare this steady-state formulation with the more general time-dependent one ([3]) we see that the steady-state equations are obtained by setting to zero all partial time derivatives in the three time-dependent subproblems. Notice that, in the steady-state case, we only use the ALE mapping to move from the undeformed to the final deformed configuration of the fluid domain, and we do not have to compute the ALE fluid domain velocity. Moreover, in the time-dependent formulation, there is another input to the fluid system, which is the solid velocity at the boundary, that is now equal to zero.

Intracranial stents as porous media. To model a porous medium stent, we follow the approch given in [2]. We assume a simple homogeneous porous medium which can be modeled by the addition of a momentum source term to the standard fluid flow equations. The pressure gradient can be expressed using the Darcy-Forchheimer equation, which can be averaged as

$$-\frac{\Delta p}{\Delta e} = \Big(\frac{\mu}{\alpha}u + \frac{1}{2}C_2\rho^f u^2\Big), \tag{20}$$

or

$$-\Delta p = bu + au^2\ , \tag{21}$$

to measure the pressure drop between the sides of the stent walls. Here, u is the average velocity, α is the permeability, C_2 is the inertial resistance factor, and Δe is the thickness of the porous medium domain. The coefficients a and b depend on the flow diverter placement in the aneurysm neck. If the aneurysm geometry requires the stent to be placed parallel to the flow, we observe low exchange of blood between the parent artery and the aneurysm cavity. This is because the flow inside the aneurysm dome is created by friction from the parent artery flow. When blood flow points directly into the aneurysm, then the flow diverter is placed perpendicularly to the flow. In this case an intense fluidic exchange between the parent artery and the aneurysm is observed. These two situations are completely different from a fluid mechanics point of view, and Eq. (21) needs to reflect this difference. We use the coefficients a and b provided in [2], which are

$$a = 1452 \ \text{ and } \ b = 4188 \quad \text{for stents placed parallel to flow direction,} \tag{22}$$

$$a = 367.08 \ \text{ and } \ b = 281.35 \ \text{ for stents placed perpendicularly to flow direction.} \tag{23}$$

From (20) and (21), the coefficients of the permeability α and the drag factor C_2 can consequently be obtained as

$$C_2 = \frac{2a}{\rho\Delta e} \quad \text{and} \quad \alpha = \frac{\mu}{b}\Delta e\ . \tag{24}$$

3 MONOLITHIC NEWTON-KRYLOV SOLVER

In a monolithic formulation, we define three unknowns (displacement, velocity and pressure) in a piecewise fashion at each point of the Eulerian domain Ω as

$$\mathbf{d} = \begin{cases} \mathbf{d}^s \text{ in } \Omega^s \\ \mathbf{d}^i \text{ in } \Gamma^i \\ \mathbf{d}^f \text{ in } \Omega^f \end{cases}, \quad \mathbf{u} = \begin{cases} \mathbf{u}^s \text{ in } \Omega^s \\ \mathbf{u}^i \text{ in } \Gamma^i \\ \mathbf{u}^f \text{ in } \Omega^f \end{cases}, \quad \mathbf{p} = \begin{cases} p^s \text{ in } \Omega^s \\ p^f \text{ in } \Omega^f \end{cases},$$

enforcing continuity across the fluid-solid interface only for the displacement and the velocity. The weak formulation of the resulting system is discretized using appropriate finite element spaces and the corresponding Jacobian matrix is obtained by an exact Newton linearization implemented by automatic differentiation ([8]). The solution of the linear systems is performed using a GMRES solver preconditioned by a geometric multigrid algorithm. The smoother is of modified Richardson type, in turn preconditioned by a restricted additive Schwarz method. The coarse grid correction problem is dealt with by a direct solver of the monolithic system.

Structure of the Jacobian. Let $\mathbf{J}^{(k)}$ denote the exact Jacobian at a nonlinear step k. Ordering the variables as

$$\left[\mathbf{d}^s\, \mathbf{d}^i\, \mathbf{d}^f \,\middle|\, \mathbf{u}^s\, \mathbf{u}^i\, \mathbf{u}^f \,\middle|\, p^s\, p^f\, \right]^\intercal \tag{25}$$

we consider the Jacobian to have the following block structure

$$\mathbf{J}^{(k)} = \left[\begin{array}{ccc||ccc||cc} S^{\mathbf{d^s}}_{\mathbf{d^s}} & S^{\mathbf{d^s}}_{\mathbf{d^i}} & 0 & 0 & 0 & 0 & S^{\mathbf{d^s}}_{p^s} & 0 \\ I^{\mathbf{d^i}}_{\mathbf{d^s}} & I^{\mathbf{d^i}}_{\mathbf{d^i}} & I^{\mathbf{d^i}}_{\mathbf{d^f}} & I^{\mathbf{d^i}}_{\mathbf{u^s}} & I^{\mathbf{d^i}}_{\mathbf{u^i}} & I^{\mathbf{d^i}}_{\mathbf{u^f}} & I^{\mathbf{d^i}}_{p^s} & I^{\mathbf{d^i}}_{p^f} \\ 0 & A^{\mathbf{d^f}}_{\mathbf{d^i}} & A^{\mathbf{d^f}}_{\mathbf{d^f}} & 0 & 0 & 0 & 0 & 0 \\ \hline\hline 0 & 0 & 0 & K^{\mathbf{u^s}}_{\mathbf{u^s}} & 0 & 0 & 0 & 0 \\ 0 & 0 & 0 & 0 & K^{\mathbf{u^i}}_{\mathbf{u^i}} & 0 & 0 & 0 \\ 0 & F^{\mathbf{u^f}}_{\mathbf{d^i}} & F^{\mathbf{u^f}}_{\mathbf{d^f}} & 0 & F^{\mathbf{u^f}}_{\mathbf{u^i}} & F^{\mathbf{u^f}}_{\mathbf{u^f}} & 0 & F^{\mathbf{u^f}}_{p^f} \\ \hline\hline V^{p^s}_{\mathbf{d^s}} & V^{p^s}_{\mathbf{d^i}} & 0 & 0 & 0 & 0 & 0 & 0 \\ 0 & W^{p^f}_{\mathbf{d^i}} & W^{p^f}_{\mathbf{d^f}} & 0 & W^{p^f}_{\mathbf{u^i}} & W^{p^f}_{\mathbf{u^f}} & 0 & 0 \end{array}\right] \begin{array}{l} \text{Momentum Solid} \\ \text{Momentum Interface} \\ \text{Kinematic fluid} \\ \text{Kinematic Solid} \\ \text{Kinematic Interface} \\ \text{Momentum Fluid} \\ \text{Continuity Solid} \\ \text{Continuity Fluid} \end{array} \tag{26}$$

Equations and unknowns are ordered following a field-ordering approach as in [7]. It is important to notice that different orderings, though equivalent mathematically, can have a significant effect on the convergence properties and computational time of the solver, especially in the parallel setting.

Geometric Multigrid preconditioner. As a preconditioner to the outer monolithic GMRES iteration, we consider the action of geometric multigrid. Let $\mathbf{\Phi}(\Omega_{h_l})$ and $\mathbf{\Psi}(\Omega_{h_l})$ be the finite element spaces associated to each level of the triangulation $\{\Omega_{h_l}\}_{l=1}^{L}$ with

relative mesh sizes h_l. The *prolongation* I_{l-1}^{l} and *restriction* I_{l}^{l-1} operators

$$I_{l-1}^{l} : \mathbf{\Phi}(\mathbf{\Omega_{h_{l-1}}}) \times \mathbf{\Phi}(\mathbf{\Omega_{h_{l-1}}}) \times \mathbf{\Psi}(\mathbf{\Omega_{h_{l-1}}}) \to \mathbf{\Phi}(\mathbf{\Omega_{h_l}}) \times \mathbf{\Phi}(\mathbf{\Omega_{h_l}}) \times \mathbf{\Psi}(\mathbf{\Omega_{h_l}}) \,, \tag{27}$$

$$I_{l}^{l-1} : \mathbf{\Phi}(\mathbf{\Omega_{h_l}}) \times \mathbf{\Phi}(\mathbf{\Omega_{h_l}}) \times \mathbf{\Psi}(\mathbf{\Omega_{h_l}}) \to \mathbf{\Phi}(\mathbf{\Omega_{h_{l-1}}}) \times \mathbf{\Phi}(\mathbf{\Omega_{h_{l-1}}}) \times \mathbf{\Psi}(\mathbf{\Omega_{h_{l-1}}}) \tag{28}$$

are defined as the natural injection from the coarse to the fine space, and the adjoint of I_{l-1}^{l} with respect to the L^2 inner product, respectively. Clearly, the matrix representations of these operators, $\mathbf{I}_{l-1}^{l}$ and $\mathbf{I}_{l}^{l-1}$, depend on the block row ordering of the Jacobian (Eq. (26)), so that a different Jacobian structure affects the structure of $\mathbf{I}_{l-1}^{l}$ and $\mathbf{I}_{l}^{l-1}$. The block structures of the prolongation and restriction operators are

$$\mathbf{I}_{l}^{l-1} = \left[\begin{array}{ccc||ccc||cc} R_{\mathbf{d^s}}^{\mathbf{d^s}} & 0 & 0 & 0 & 0 & 0 & 0 & 0 \\ R_{\mathbf{d^s}}^{\mathbf{d^i}} & R_{\mathbf{d^i}}^{\mathbf{d^i}} & 0 & 0 & 0 & R_{\mathbf{u^f}}^{\mathbf{d^i}} & 0 & 0 \\ 0 & 0 & R_{\mathbf{d^f}}^{\mathbf{d^f}} & 0 & 0 & 0 & 0 & 0 \\ \hline\hline 0 & 0 & 0 & R_{\mathbf{u^s}}^{\mathbf{u^s}} & 0 & 0 & 0 & 0 \\ 0 & 0 & 0 & R_{\mathbf{u^s}}^{\mathbf{u^i}} & R_{\mathbf{u^i}}^{\mathbf{u^i}} & 0 & 0 & 0 \\ 0 & 0 & 0 & 0 & 0 & R_{\mathbf{u^f}}^{\mathbf{u^f}} & 0 & 0 \\ \hline\hline 0 & 0 & 0 & 0 & 0 & 0 & R_{p^s}^{p^s} & 0 \\ 0 & 0 & 0 & 0 & 0 & 0 & 0 & R_{p^f}^{p^f} \end{array}\right], \quad \mathbf{I}_{l-1}^{l} = \left[\begin{array}{ccc||ccc||cc} P_{\mathbf{d^s}}^{\mathbf{d^s}} & P_{\mathbf{d^s}}^{\mathbf{d^i}} & 0 & 0 & 0 & 0 & 0 & 0 \\ 0 & P_{\mathbf{d^i}}^{\mathbf{d^i}} & 0 & 0 & 0 & 0 & 0 & 0 \\ 0 & P_{\mathbf{d^f}}^{\mathbf{d^i}} & P_{\mathbf{d^f}}^{\mathbf{d^f}} & 0 & 0 & 0 & 0 & 0 \\ \hline\hline 0 & 0 & 0 & P_{\mathbf{u^s}}^{\mathbf{u^s}} & P_{\mathbf{u^s}}^{\mathbf{u^i}} & 0 & 0 & 0 \\ 0 & 0 & 0 & 0 & p_{\mathbf{u^i}}^{\mathbf{u^i}} & 0 & 0 & 0 \\ 0 & 0 & 0 & 0 & 0 & P_{\mathbf{u^f}}^{\mathbf{u^f}} & 0 & 0 \\ \hline\hline 0 & 0 & 0 & 0 & 0 & 0 & P_{p^s}^{p^s} & 0 \\ 0 & 0 & 0 & 0 & 0 & 0 & 0 & P_{p^f}^{p^f} \end{array}\right].$$

Richardson-Schwarz smoother. In the smoothing process, we first partition the whole domain into the fluid and solid subregions, and then we further divide each subregion into smaller non-overlapping blocks $\Omega_k, k = 1, ..., N$. On each subdomain Ω_k we construct a subdomain preconditioner $\mathbf{B_k}$, which is a restriction of the Jacobian matrix $\mathbf{J}$, that is, it contains entries from $\mathbf{J}$ corresponding to the degrees of freedom (DOFs) contained in the corresponding subdomain Ω_k. The exchange of information between blocks is guaranteed by the fact that the support of the test function associated to the displacement and velocity DOFs extends to the neighboring elements. The restricted version of the additive Schwarz (ASM) preconditioner used in the Richardson scheme for the FSI Jacobian system is

$$\mathbf{B}^{-1} = \sum_{k=1}^{N} (\mathbf{R}_k^0)^T \mathbf{B}_k^{-1} (\mathbf{R}_k^\delta) \,. \tag{29}$$

With $\mathbf{R_k}$ we indicate a restriction matrix which maps the global vector of degrees of freedom to those belonging to the subdomain Ω_k. Furthermore, $\mathbf{R_k^0}$ is a restriction matrix that does not include the overlap while $\mathbf{R_k^\delta}$ does.

4 FSI BENCHMARKING: 2D SIMULATIONS

The following 2D simulations of a cerebral aneurysm are based on a 2D hemodynamic model problem from [10]. We start by considering a mesh without stents, and then move to three cases where such devices are included. Figure 1 shows the four configurations.

Stents are flexible, self-expanding porous tubular meshes made of stainless steel or other alloys and are characterized by very thin wires ($30 - 100\mu m$). As a consequence, in 2D flow diverters can be simplified as cutplanes from 3D configurations, so as circular shapes. This is the approach used in the second and third configuration. The difference beetween these two cases is in the number of struts that compose the stent, to be precise five and eleven struts, respectively. In both configurations, the wires have a diameter of approximately $60\mu m$. We conclude our simulations with a case where a stent is modeled as a porous medium. The porous medium strip placed on the neck of the aneurysm has a width of approximately $60\mu m$ ($\Delta e = 60\mu m$). Since the stent is placed parallel to the flow, we know from section 2.4 that the coefficients used to represent the pressure drop are $a = 1452$ and $b = 4188$. In all cases, hybrid meshes are employed. Quads are mainly used to mesh the channel and the arterial wall of the geometry, while triangles are employed in the aneurysm bulge.

Mechanical properties and boundary conditions. Blood is known to be non-Newtonian in general, but, for cerebral aneurysms, treatment of blood as Newtonian does not alter the computational results compared to treating it as non-Newtonian, as Cebral et al. showed in [5]. In this work, we assume blood to be Newtonian. The density and viscosity of the blood were set to 1035 kg/m^3 and $3.5 \times 10^3 Pa \cdot s$, respectively. The following material parameters were used in the simulation: the density of the solid was 1120 kg/m^3, Young's modulus and Poisson's ratio were $1.0MPa$ and 0.5, respectively. In the the porous medium configuration, we considered its width (thickness in 3D) to be $60\mu m$. The boundary conditions we consider are as in [10]. Blood flows from the right to the left part of the channel, and the velocity profile is defined as parabolic inflow

$$v^f(0, y) = 0.05\,(y - 6)(y - 8). \tag{30}$$

Pressure conditions representing the resistance due to the peripheral arterial network are not taken into account in this 2D model, therefore $p = 0$ has been imposed as outflow condition at the lower left part of the artery. The no-slip condition is prescribed for the fluid on the other boundary parts. The boundary displacements at the inlet and outlet of the artery are set to zero.

Numerical results. In all the four simulations we performed, we considered the same physical parameters and boundary conditions. Table 1 shows the changes of pressure, velocity and volume in the aneurysm dome for all four cases. The five struts configuration is the one that allows a greater dicrease in both volume and pressure. We see that doubling the number of struts, the relative difference in volume increases by 28.29% compared to the previous case, while the average pressure increases by 20.75%. This is suggesting that for a given aneurysm geometry, stents with different designs may give different results. Figure 2 shows the pressure distribution for these two configurations. In both cases, the highest pressure point is located on the aneurysm neck, but for the 5 struts geometry this point is at the left of the neck, while for the 11 struts configuration it is at the far right. Pressure values at these points are different as well. We also observe that the behavior

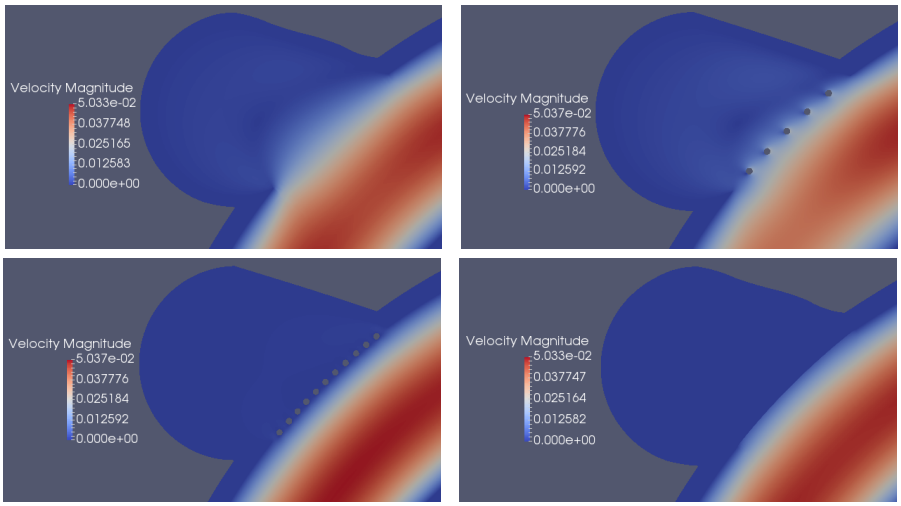

Figure 1: Magnitude Velocity for the four 2D Configurations: no stents (top left), stent with five struts (top right), stent with eleven struts (bottom left), stent modeled as a porous medium (bottom right).

Table 1: volume, pressure and velocity in 2D configurations

	average pressure	average velocity	relative difference in volume
no stents	1.0794	1.4264	0.0166
5 struts	0.7632	1.2029	0.0109
11 struts	0.9630	0.0927	0.0152
porous	0.9955	0.0135	0.0150

of the eleven struts configuration is very similar to the porous medium case in terms of volume and pressure. Average velocities show that these two configurations are the ones that allow a greater decrease of blood velocity inside the aneurysm dome. The similarity beetween the porous medium case and the 11 struts configuration shows the validity of the porous medium approach. Figure 1 shows the velocity magnitude at the aneurysm neck and dome for all four configurations. As we pointed out, the porous medium case resembles the real stent configuration with 11 wires.

5 FSI BENCHMARKING: 3D SIMULATIONS

The cerebral aneurysm considered in this section is a 3D extension of the 2D geometry analyzed above. To make the shape more realistic, changes have been made to the aneurysm dome, based on a real aneurysm view proposed in [10]. We assumed the aneurismal wall to be uniform and equal to $0.25mm$. Two configurations have been considered, one without stents and a second one where such devices are included and modeled as a

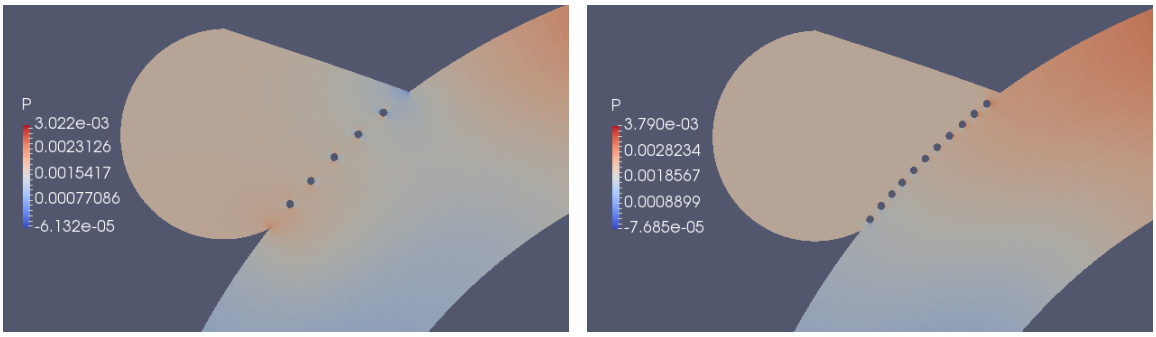

Figure 2: 2D Configurations: pressure distribution for the five struts stent configuration (right), pressure distribution for the eleven struts stents configuration (left).

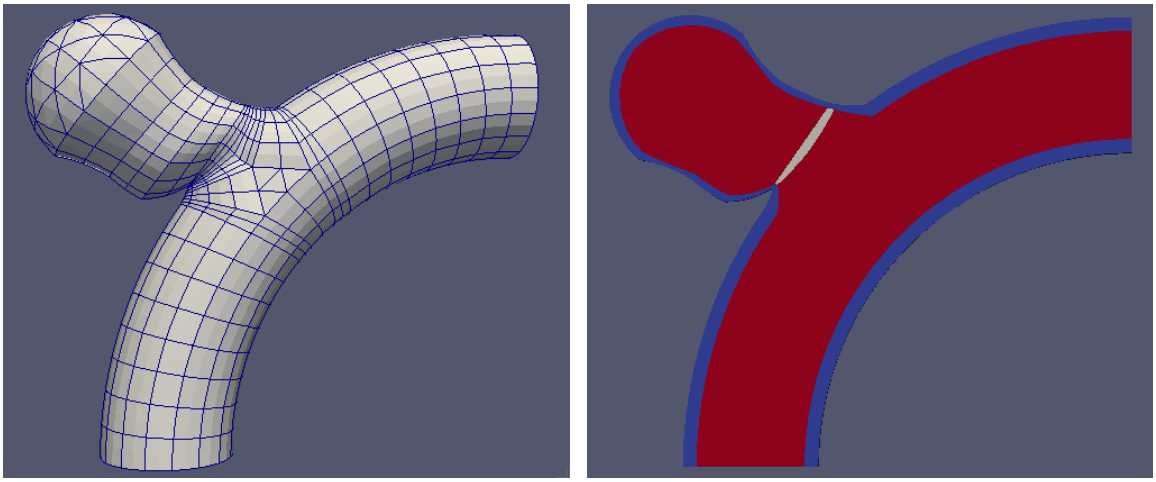

Figure 3: 3D Configurations: geometry with mesh (left), section of the 3D geometry to show the porous medium disk that simulates the intracranial stent.

porous medium disk (Figure 3). Such disk placed on the neck of the aneurysm has a thickness of approximately $112\mu m$. In both our geometries (with and without stents), hybrid meshes are employed. Wedges are needed to mesh the artery lumen, and hexes are used for the arterial wall. Tets are mainly employed in the aneurysm dome.

Mechanical properties and boundary conditions. Except for the Young Modulus value, the physical parameters are the same used in the 2D simulations, both for blood and the elastic artery wall. To clearly see the artery and the aneurysm pulse we considered $0.012MPa$ as our Young modulus value. At the inlet the velocity profile is defined as parabolic inflow and as outflow condition $p = 0$ has been imposed at the lower left part of the artery. The boundary displacements at the inlet and outlet are set to zero.

Numerical results. In both simulations we performed, we considered the same physical parameters and boundary conditions. Table 2 shows the changes of pressure, velocity

and volume in the aneurysm dome for all four cases. The velocity magnitudes at the aneurysm neck and dome are shown in Figure 4. As we observed for the 2D setting, the flow rate changes after the porous medium placement causing a reduction of the velocity magnitude on the aneurysm neck and dome. Therefore the porous medium approach performs well also in a FSI environment.

Table 2: volume, pressure and velocity in 3D configurations

	average pressure	average velocity	relative difference in volume
no stents	322.6082	24.3485	0.0065
porous	323.6605	0.4756	0.0066

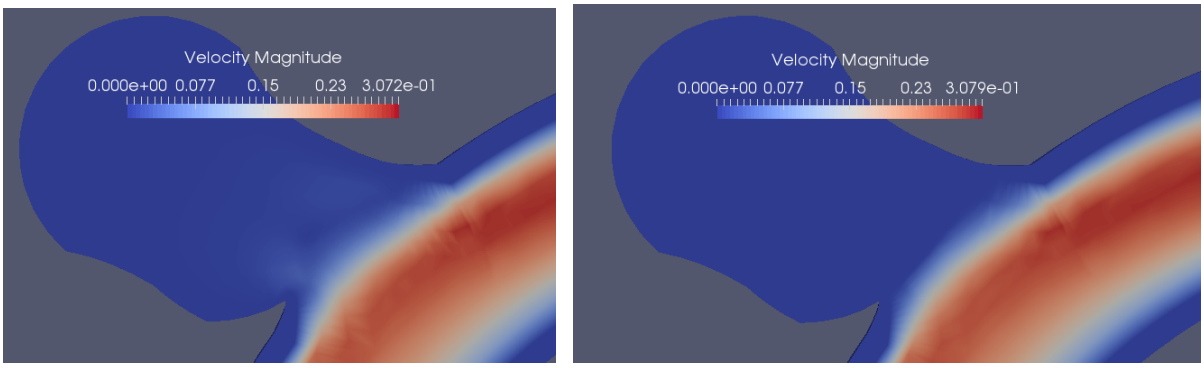

Figure 4: Magnitude Velocity for the 3D Configurations: no stents (left), porous medium (right)

6 CONCLUSION

In this paper we focused on the numerical simulation of FSI problems regarding stented intracranial aneurysms. We presented a monolithic ALE formulation assuming the fluid flow and the hyperelastic material to incompressible. We described the Newton-Krylov solver we employed where we considered the use of geometric multigrid preconditioners. From our simulations, we verified the stability and numerical efficiency of the FSI algorithm and observed that the modelization of a flow diverter as a porous medium is successful in a FSI enviroment. Morover, in the 2D simulations, the different results obtained with the 5 and 11 struts configurations highlight the prominent design dependence on flow diverters performances. Studies about stents optimization techniques can be found in [1] and [13]. In our future work, we will further investigate how to choose the porosity coefficients for any general stent.

REFERENCES

[1] Hitomi Anzai, Makoto Ohta, Jean-Luc Falcone, and Bastien Chopard. Optimization of flow diverters for cerebral aneurysms. *Journal of Computational Science*, 3(1):1–7, 2012.

[2] L Augsburger, P Reymond, DA Rufenacht, and N Stergiopulos. Intracranial stents being modeled as a porous medium: flow simulation in stented cerebral aneurysms. *Annals of biomedical engineering*, 39(2):850–863, 2011.

[3] Eugenio Aulisa, Simone Bnà, and Giorgio Bornia. A monolithic ALE Newton-Krylov solver with Multigrid-Richardson-Schwarz preconditioning for incompressible Fluid Structure Interaction. *Submitted to Siam Journal on Scientific Computing*, 2017.

[4] Satish Balay, J Brown, Kris Buschelman, Victor Eijkhout, W Gropp, D Kaushik, M Knepley, L Curfman McInnes, B Smith, and Hong Zhang. PETSc users manual revision 3.3. *Computer Science Division, Argonne National Laboratory, Argonne, IL*, 2012.

[5] Juan R Cebral, Marcelo Adrián Castro, Sunil Appanaboyina, Christopher M Putman, Daniel Millan, and Alejandro F Frangi. Efficient pipeline for image-based patient-specific analysis of cerebral aneurysm hemodynamics: technique and sensitivity. *IEEE transactions on medical imaging*, 24(4):457–467, 2005.

[6] Jean Donea, S Giuliani, and Jean-Pierre Halleux. An arbitrary Lagrangian-Eulerian finite element method for transient dynamic fluid-structure interactions. *Computer methods in applied mechanics and engineering*, 33(1-3):689–723, 1982.

[7] Miguel Ángel Fernández and Marwan Moubachir. A Newton method using exact Jacobians for solving fluid–structure coupling. *Computers & Structures*, 83(2):127–142, 2005.

[8] Robin J Hogan. ADEPT fast automatic differentiation library for C++: User guide.

[9] Mudassar Razzaq, Hogenrich Damanik, Jaroslav Hron, Abderrahim Ouazzi, and Stefan Turek. FEM multigrid techniques for fluid–structure interaction with application to hemodynamics. *Applied Numerical Mathematics*, 62(9):1156–1170, 2012.

[10] Stefan Turek, J Hron, Martin Madlik, Mudassar Razzaq, Hilmar Wobker, and Jens F Acker. Numerical simulation and benchmarking of a monolithic multigrid solver for fluid-structure interaction problems with application to hemodynamics. In *Fluid Structure Interaction II*, pages 193–220. Springer, 2011.

[11] Thomas Wick. Fluid-structure interactions using different mesh motion techniques. *Computers & Structures*, 89(13):1456–1467, 2011.

[12] Hilmar Wobker and Stefan Turek. Numerical studies of Vanka-type smoothers in computational solid mechanics. *Advances in Applied Mathematics and Mechanics*, 1(1):29–55, 2009.

[13] Y Zhang, W Chong, and Y Qian. Investigation of intracranial aneurysm hemodynamics following flow diverter stent treatment. *Medical engineering & physics*, 35(5):608–615, 2013.